Research Article

Frank Rutz*, Rolf Aidam, Henning Heußen, Wolfgang Bronner, Robert Rehm, Matthias Benecke, Alexander Sieck, Simon Brunner, Benjamin Göhler and Peter Lutzmann

InGaAs APD matrix sensors for SWIR gated viewing

https://doi.org/10.1515/aot-2019-0039
Received June 7, 2019; accepted August 19, 2019; previously published online September 10, 2019

Abstract: Short-wavelength infrared (SWIR) detection systems are increasingly in demand for surveillance, reconnaissance, and remote sensing applications. Eye-safe SWIR lasers can be utilized for active imaging systems with high image contrast and long detection range. The gated-viewing (GV) technique using short-pulse lasers and fast-gated cameras in the nanosecond range enables utilizing the distance information in addition to the signal intensity of the acquired images. The InGaAs material system is very well suited for the fabrication of high-performance SWIR photodetectors providing a typical cutoff wavelength of 1.7 μm, which covers the emission lines of available laser sources at typical telecom wavelengths around 1.55 μm. However, the usually short integration times needed for GV leads to very small photosignals. We report on the development of SWIR avalanche photodetector (APD) arrays with 640 × 512 pixels and 15 μm pixel pitch based on the InGaAs material system. The InGaAs-APD focal plane arrays have been successfully integrated into SWIR cameras which yield gain values of $M \approx 10$ on camera level at a reverse bias voltage around 21 V and are the first InGaAs-based SWIR cameras worldwide providing a 640 × 512 image format and utilizing avalanche gain for signal amplification. The camera performance is demonstrated by SWIR laser GV sample images.

***Corresponding author: Frank Rutz,** Fraunhofer Institute for Applied Solid State Physics IAF, Tullastrasse 72, 79108 Freiburg, Germany, e-mail: frank.rutz@iaf.fraunhofer.de
Rolf Aidam, Henning Heußen, Wolfgang Bronner and Robert Rehm: Fraunhofer Institute for Applied Solid State Physics IAF, Tullastrasse 72, 79108 Freiburg, Germany
Matthias Benecke and Alexander Sieck: AIM Infrarot-Module GmbH, Theresienstrasse 2, 74072 Heilbronn, Germany
Simon Brunner, Benjamin Göhler and Peter Lutzmann: Fraunhofer Institute of Optronics, System Technologies, and Image Exploitation IOSB, Gutleuthausstrasse 1, 76275 Ettlingen, Germany

www.degruyter.com/aot

Keywords: avalanche photodiode; focal plane array; gated viewing; short-wavelength infrared.

1 Introduction

Active infrared imaging is an increasingly demanded technique for surveillance, reconnaissance, and remote sensing applications. Especially, if short-pulsed laser sources are used for the illumination of the observed scene, the time of flight of the forth and back propagating laser pulses can be utilized for achieving additional range information. For this so-called light detection and ranging (LIDAR) technique, long detection ranges up to several 10 km [1] can be achieved by using powerful lasers and highly sensitive sensors.

The most straight-forward approach is the combination of a low-divergence laser beam and a single detector element that are both directed at the same target and are rapidly scanned across the observed scene in order to acquire a two-dimensional image. Fast moving objects, however, appear distorted or may even be missed if their velocity cannot be neglected compared to the scanning speed of the LIDAR optical system. This issue is circumvented via flash illumination of the complete scene with an expanded laser beam and capturing of every LIDAR image with a two-dimensional camera in a single-shot. Yet, this flash LIDAR approach requires high laser pulse energy and a fast detector focal plane array (FPA) with high photon responsivity as well as the ability to temporarily resolve the photon arrival time.

For eye-safety reasons [2], the usage of lasers in the short-wavelength infrared (SWIR) with wavelengths above 1400 nm are beneficial in order to make high detection ranges accessible by a sufficiently high intense laser emission. Still, the signal intensity from the returning photons at the detector is extremely low and scales inversely proportional with the square of the detection range [3]. Therefore, LIDAR imaging systems usually comprise avalanche photodiodes (APDs) operated in

linear mode or even single-photon avalanche photodiodes (SPADs) operated in the Geiger-mode [4] in order to determine the distance of objects in the observed scene with maximum detection range and resolution via the time of flight (ToF) of the scattered or reflected photons. Especially SPADs for the SWIR spectral range based on the InGaAs/InP semiconductor material system are quite challenging to fabricate as detector arrays with high spatial resolutions. Typical 2D array sizes of 32×32 [5] to 128×32 [6] are still far away from (sub-)megapixel image formats.

A special variant of flash LIDAR is gated viewing (GV) [7]. In GV, the integration period of the camera sensor is fast gated with respect to the trigger of the laser emission. Instead of ToF images, in which each pixel represents the distance information via the arrival time of the first photon triggering an avalanche breakdown event, GV images resemble certain distance interval, or range slice, corresponding to the switching times of the gate window. With nanosecond timing constants, sub-meter distance resolutions can be achieved. The strength of GV lies in its ability to generate silhouette images of the objects that are located within the selected range slice [8, 9]. Furthermore, the photo-generated charge accumulation within the read-out integrated circuit (ROIC) of GV image sensors is much less sophisticated than the time-to-signal electronic circuits of ToF LIDAR systems, enabling pixel pitches of GV-FPAs as small as 15 µm.

Till date, the electron bombarded (EB) CMOS sensor is widely considered as the state-of-the-art technology for high-performance, SWIR-GV systems. This technology is based on an InGaAs/InP semiconductor photocathode in proximity to a high-resolution backside-thinned CMOS chip anode. The electrons emitted by the photocathode are directly injected in the electron bombarded mode into the CMOS anode, where the electrons are collected, amplified, and read-out of the CMOS sensor [10]. However, the EB-CMOS sensor is patented [11, 12], under export control, and subjected to the United States' International Traffic in Arms Regulations. The restricted availability causes a significant demand for alternative SWIR-GV sensor systems.

In this paper, we have reported the development of a GV system in the eye-safe SWIR spectral range with high spatial resolution, high distance resolution, and high detection range. For the detector material of the FPA, two technological paths were conducted in parallel: While one collaboration partner, AIM Infrarot-Module GmbH, developed an APD sensor in the HgCdTe material system [13] we focused in the following on the development of an InGaAs-based APD sensor fabricated at Fraunhofer IAF. The InGaAs detector arrays were hybridized with the same ROICs (except for the inverted polarity) as their counterpart HgCdTe detectors at AIM. After integration into a stirling-cooled camera assembly, the cameras were setup into a GV system and characterized at Fraunhofer IOSB. The GV ROIC and the GV system have been developed by AIM. A commercial Nd:YAG laser with optical parametric oscillator, providing an emission wavelength of 1570 nm, an average pulse length of 8 ns, and a maximum pulse energy of 60 mJ, was selected as laser source and combined with a square flat-top beam homogenizer [14].

2 SWIR sensor development

The project aimed at developing a FPA with a format of 640×512 pixels. The pixel pitch of 15 µm just provides enough area for the pixel-level circuit of the custom-made silicon ROIC for featuring a capacitive trans-impedance amplifier as input stage, a 200-MHz fast phase-locked-loop clock generator for short integration times, and a GV mode with optional ability for correlated double sampling (CDS). The charge handling capacity of the ROIC accommodates 120 000 electrons. The read-out noise was rated as approximately 80 electrons without CDS. Four output channels allow for a maximum full frame rate of 100 Hz. More details on the GV-ROIC can be found elsewhere [13]. Since the integration times in GV are usually very short in the range of a few ns to several 100 ns, the dark current of the photodetectors is not the main contribution to the overall system noise. Thus, APDs are beneficial for the image contrast in GV systems, because their photosignal amplification due to the avalanche multiplication gain outbalances the intrinsically higher dark-current characteristics compared to classical *pin* photodiodes.

2.1 InGaAs avalanche photodiodes

InGaAs is the semiconductor material of choice for many optoelectronic devices in the SWIR spectral range. When grown on lattice-matched InP-substrates, InGaAs photodetectors reveal low dark currents, a cutoff wavelength of 1.7 µm, and a peak responsivity between 1.5 and 1.6 µm [15], where typical emission wavelengths of available high-power lasers reside. In contrast to HgCdTe, InGaAs-based photodetectors can rely on a mature III/V rather than a more delicate II/VI compound semiconductor process technology.

In APDs, signal amplification is achieved by impact ionization of charge carriers in a high-field domain. Yet, this high electric field would cause high tunnelling dark currents in the depletion region of classical InGaAs *pin* diodes under reverse bias voltage due to the relatively low bandgap of InGaAs. For this reason, InGaAs-based APDs nowadays comprise a sophisticated heterostructure with higher-bandgap materials in order to shift the high-field domain from the low-bandgap InGaAs absorber region into a high-bandgap multiplication layer. Further intermediate charge and grading layers take care of the optimal doping profile and the reduction of the barrier effect for the photo-generated carriers due to band offsets.

The high operating voltage of an APD is also difficult to handle by the ROIC, in particular when it comes to high-resolution FPAs for imaging applications. In fact, a significant gain at operating voltages up to 20 V is desirable as of today. For this reason, we decided on an APD heterostructure comprising an InGaAs absorption layer, InAlAs charge and multiplication layers, and linearly graded InAlGaAs layers between the InGaAs and InAlAs layers.

The thickness of the InGaAs photon absorption layer of 1 µm together with the absorption coefficient of InGaAs at a wavelength of 1.57 µm of approximately 700 cm^{-1} [16] leads to an unamplified quantum efficiency (QE) of 75% in double-pass configuration as can be assumed for backside illuminated FPAs. This relatively high QE value is a clear advantage compared to the QE of 25% as rated for the EB-CMOS technology [17].

The complete layer structure was grown on lattice-matched 3-inch InP substrate wafers by molecular beam epitaxy [18]. During the epitaxy development, it turned out that the doping concentration [19] and thickness [20] of the InAlAs charge layer and its neighboring InAlGaAs grading layer play a crucial role in the *I-V* characteristics of the APD. Within several iteration loops of epitaxy, test structure device processing, and electro-optical characterization, we managed to reduce the breakdown voltage of the InGaAs/InAlAs APDs from 47 V [18] to 31 V, 23 V [21], and finally 19 V [22].

2.2 Focal plane array development

We followed the approach of a mesa process for the front-side process technology, because the mesa-etch process has important advantages over the planar process for applications using detector arrays. Due to the physically separated pixels of a mesa-etched structure, optical as well as electrical crosstalk between neighboring pixels can be almost neglected. Next, layer thicknesses and doping levels can be controlled much better during epitaxial growth compared to the diffusion process for the upper layers of a planar structure. Especially planar processed APDs usually require floating guard rings in order to avoid edge breakdown, which is caused by the curved diffusion front of the Zn-dopant [23, 24]. This fact prevents the fabrication of such small pixels for a high-resolution detector array, as it is possible with the mesa-etch process. Camera detector arrays as well as test structures with various sizes and geometries for materials and process characterization are processed using an inductively coupled plasma dry-etching process, a consecutive wet-chemical etch process, and a dielectric passivation of the sidewall in order to minimize surface-related dark current due to lattice damage. With a nominal trench width of 2 µm between the pixels, our FPAs with 640×512 pixels at a pixel pitch of 15 µm provide a fill factor as high as 75% [25].

For imaging applications, the removal of the substrate is advantageous in order to reduce absorption losses and blurring. For this purpose, the detector chips were treated in a backside process after flip-chip hybridization with the ROIC, by mechanical grinding and a subsequent two-step wet-chemical etch process [18]. Finally, a single-layer $SiON_x$ anti-reflection coating was applied in order to enhance the external quantum efficiency of the FPA.

Figure 1A shows the photograph of the opened SWIR-GV camera with $f = 600$ mm lens optics, two folding mirrors, and the integrated detector cooler assembly. The InGaAs-APD detector chip, as depicted in Figure 1B, constitutes the core of the camera. A close-up image by secondary-electron microscopy (SEM) of the InGaAs-APD detector array is presented in Figure 1C.

3 Gated-viewing results

The resulting FPAs were integrated into SWIR-GV cameras. The camera of the GV demonstrator was equipped with optics with a focal length of $f = 600$ mm, an F/# of 3, and a field of view of FOV = 0.91° (horizontal) × 0.73° (vertical), respectively. Outdoor tests have been performed by Fraunhofer IOSB.

3.1 Multiplication gain

The multiplication gain factor of APD cameras is determined by evaluating the voltage dependent average signal of a homogeneously illuminated FPA in a laboratory setup. The camera-level gain curve of a recent

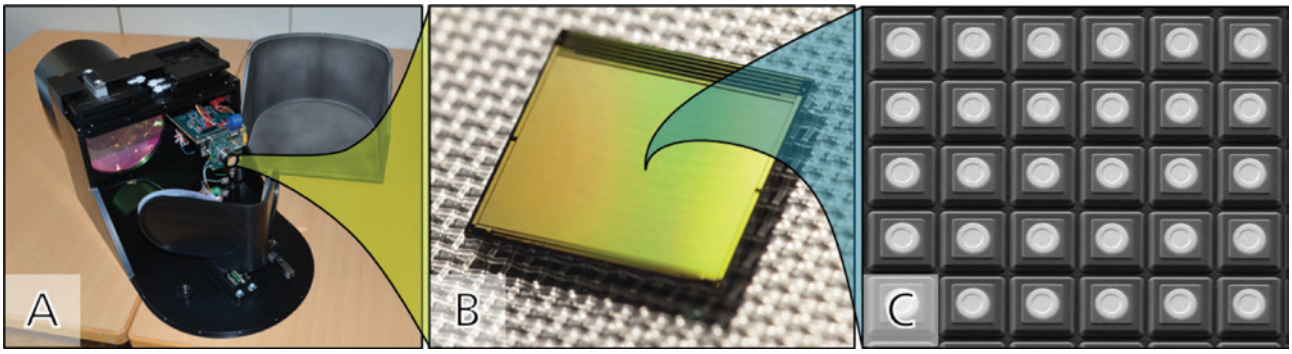

Figure 1: Photographs of the SWIR-GV camera (A) and the InGaAs-APD detector array (B). SEM image of a part of the InGaAs-APD detector array (C), showing individual mesa pixels with a fill factor of 75%.

InGaAs-APD FPA operated at 140 K is presented in Figure 2A. A multiplication gain $M > 1$ sets in just above a reverse bias voltage of 13 V and reaches $M = 10$ at 21 V. SWIR-GV images of a rooftop with a chimney at a distance of approximately 200 m have been taken with different bias voltages applied to the common substrate contact of the APD detector matrix. The gating parameters for these GV images were an integration time of 315 ns with a delay of 1200 ns, corresponding to a selected range slice with a depth of 47.25 m starting at a distance of 180 m. The different gain values of $M = 1$ and 6 express significant differences of the image contrast that is clearly visible in Figure 2B and C, respectively. An identical grayscale mapping was used for both GV images. The optical contrast of the GV images in Figure 2B and C can be estimated by the intensity difference between the average signal level within a certain region of interest (ROI) on the brightly illuminated side of the chimney as foreground and the average signal level within another ROI on the dark sky as background. This way, the ratio of the contrast of the amplified GV image of Figure 2C to the contrast of the unamplified GV image of Figure 2B yields 5.8 in good agreement to the nominal gain factor 6 as expected from the gain-voltage characteristic in Figure 2A.

3.2 3D-scene reconstruction

The GV images in Figure 3 demonstrate the benefit of the distance information in addition to the intensity information of SWIR imaging. Figure 3A shows a GV image of two chimneys at distances of 115 m and 120 m, respectively, captured with a 115 ns, i.e. 17.25 m, long gate, starting after a delay of 730 ns, i.e. at a range of 109.5 m, and spanning both chimneys. The different distances of the two chimneys can hardly be estimated from this image. In the GV images of Figure 3B and C, the gate delays were set to 670 ns and 780 ns, so that they span only the front or the rear chimney, respectively. The gate lengths were the same as for the GV image of Figure 3A. The pulse energy of the 1570 nm laser was 50 mJ for all three GV images. The combination of several range slices can be used to generate a three-dimensional model of the observed scene [8]. A high depth resolution requires

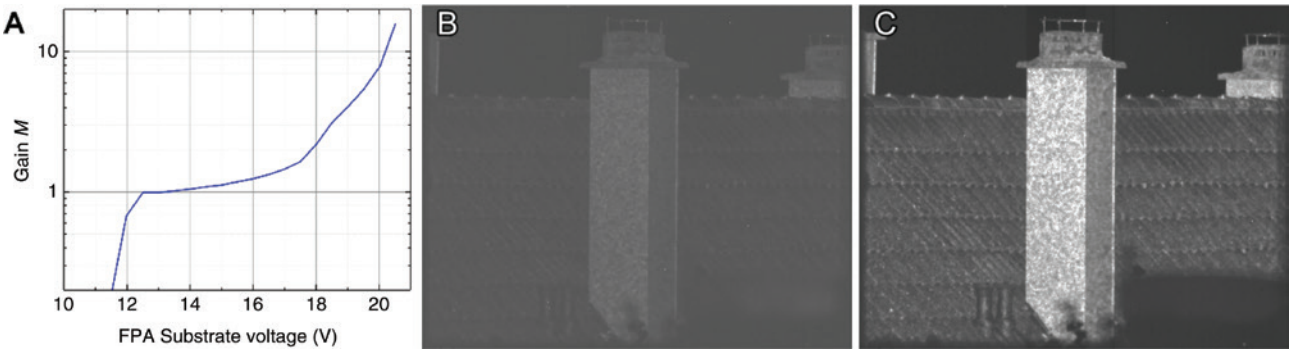

Figure 2: Camera-level gain curve of a 640×512 InGaAs-APD camera operated at 140 K (A), GV images taken with FPA substrate voltages of 13 V and 19.7 V corresponding to gain values $M = 1$ (B) and $M = 6$ (C), respectively.

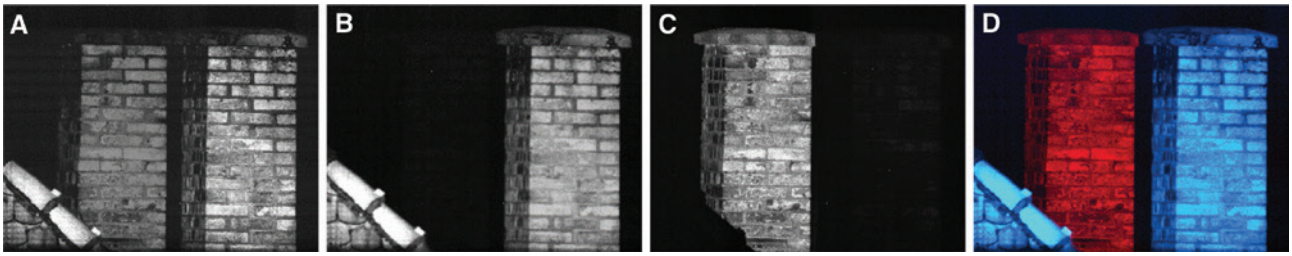

Figure 3: GV images of two chimneys at distances of 115 m and 120 m, respectively, captured with a 115 ns, i.e. 17.25 m, long gate spanning both chimneys (A), a gate set on the front chimney (B) and on the rear chimney (C) only. A superposition of the GV images B and C colour-coded in blue and red, respectively (D).

a dense, equidistant set of range slices covering the full range of interest. Nevertheless, even just two GV images can already generate a three-dimensional data set with the range information as third dimension. Figure 3D contains a superposition of the GV images B and C, which have been colour-coded in blue and red, respectively. In contrast to the single GV image of Figure 3A, the superposition of two GV images in Figure 3D gives a much better impression of the 3-dimensional scene.

3.3 Silhouette imaging

Another benefit of the range discriminating ability of GV is the generation of silhouette images. This is especially useful for the classification of persons in front of a highly cluttered background such as vegetation etc. Figure 4A shows a photograph of a person wearing camouflage clothing, close to a tree at a distance of 128 m. The GV image in Figure 4B obtained with a laser pulse energy of 25 mJ and the gate (length: 115 ns $\triangleq$ 17.25 m, delay: 850 ns $\triangleq$ 127.5 m) set just behind the person results in an image in which the person is silhouetted against the tree trunk and the wall in the background. The gate (length: 115 ns $\triangleq$ 17.25 m, delay: 790 ns $\triangleq$ 118.5 m) of the GV image in Figure 4C, however, spans the complete scene of the person, the tree trunk, and the wall in the background.

4 Conclusions

We have reported on the achievement of developing InGaAs-based APD detector arrays for SWIR GV applications. The InGaAs-APD FPAs with 640×512 pixels and 15-µm pixel pitch have been successfully integrated into SWIR cameras. With gain values of $M = 10$ on camera level at a reverse bias voltage around 21 V, these cameras are the first InGaAs-based SWIR cameras worldwide providing a 640×512 image format and utilizing avalanche gain for signal amplification. The camera performance has been demonstrated by means of SWIR-GV images with high contrast, colour-coded distance images

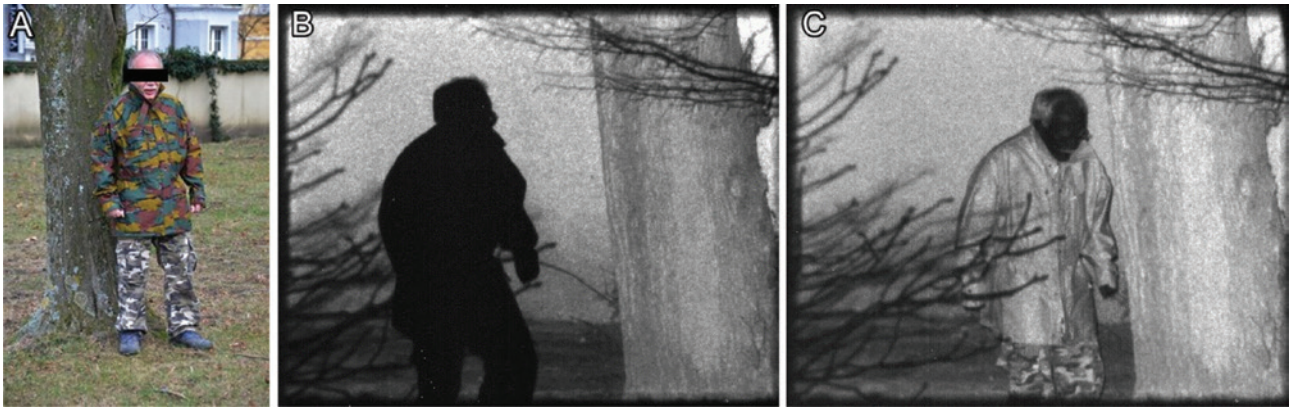

Figure 4: Photograph of a person close to a tree at a distance of 128 m (A), a GV image with the gate set just behind the person (B), and a GV image with the gate spanning the person and the tree (C).

and silhouette images of various observed scenes. The performance data of the InGaAs-APD GV sensors are essentially comparable to their HgCdTe counterpart [13] but without the need for delicate II/VI materials and process technology.

Acknowledgments: We would like to acknowledge S. Fibelkorn, T. Henkel, R. Lappe, W. Luppold, and S. Rombach for detector processing, and M. Prescher, T. Fuchs, M. Grimm, and L. Kirste for HRXRD and SIMS characterization. We also like to thank M. Finck from AIM Infrarot-Module GmbH for flip-chip hybridisation. This work has been supported by the German Federal Ministry of Defence, the Bundeswehr Technical Center WTD81, and the Bundeswehr Technical Center WTD91.

References

[1] Z. Li, X. Huang, Y. Cao, B. Wang, Y. Li, J. Zhang, Q. Zhang, C. Peng, F. Xu, and J. Pan, in Conference on Lasers and Electro-Optics, OSA Technical Digest, paper SM1N.1 (2019).
[2] DIN EN 60825-1:2015-07, 'Safety of Laser Products – Part 1: Equipment Classification and Requirements (IEC 60825-1:2014)', (2015).
[3] U. Wandinger, in 'Lidar: Range-Resolved Optical Remote Sensing of the Atmosphere', (Springer, New York, 2005).
[4] M. A. Itzler, X. Jiang, M. Entwistle, B. M. Onat and K. Slomkowski, Proc. SPIE 7681, 76810V (2010).
[5] T. Baba, Y. Suzuki, K. Makino, T. Fujita, T. Hashi, et al., Proc. SPIE 10540, 105400L (2018).
[6] X. Jiang, S. Wilton, I. Kudryashov, M. A. Itzler, M. Entwistle, et al., Proc. SPIE 10729, 107290C (2018).
[7] L. F. Gillespie, J. Opt. Soc. Am. 56, 883–887 (1966).
[8] I. Baker, D. Owton, K. Trundle, P. Thorne, K. Storie, et al., Proc. SPIE 6940, 69402L (2008).
[9] B. Göhler and P. Lutzmann, Opt. Eng. 56, 031203 (2017).
[10] Intevac, 'Photonics/EBAPS Technology', Intevac, Inc., [Online]. Available: www.intevac.com/intevacphotonics. [Accessed 8 Aug 2019].
[11] V. Aebi and J. Boyle, 'Electron Bombarded Active Pixel Sensor', US Patent 6285018, 4 Sep 2001.
[12] V. Aebi and J. Boyle, 'Electron bombarded active pixel sensor', EP Patent 1306906, 5 Oct 2011.
[13] A. Sieck, M. Benecke, D. Eich, R. Oelmaier, J. Wendler and H. Figgemeier, J. Elec. Materi. 47, 5705 (2018).
[14] M. Laurenzis, Y. Lutz, F. Christnacher, A. Matwyschuk and J. M. Poyet, Optic. Engin.51, 061302 (2012).
[15] P. Kleinow, F. Rutz, R. Aidam, W. Bronner, H. Heussen, et al., Proc. SPIE 9249, 92490X (2014).
[16] M. Levinshtein, S. Rumyantsev and M. Shur, Handbook Series on Semiconductor – Ternary and Quaternary III-V Compounds, (vol. 2, World Scientific, Singapore, 1996).
[17] Intevac, 'LIVAR M506 Datasheet', Jul 2018. [Online]. Available: www.intevac.com/intevacphotonics. [Accessed 8 Aug 2019].
[18] F. Rutz, P. Kleinow, R. Aidam, W. Bronner, L. Kirste, et al., Proc. SPIE 8896, 88960C (2013).
[19] P. Kleinow, F. Rutz, R. Aidam, W. Bronner, H. Heussen, et al., Infrared Phys. Technol. 71, 298 (2015).
[20] P. Kleinow, F. Rutz, R. Aidam, W. Bronner, H. Heussen, et al. Phys. Status Solidi A. 213, 925(2016).
[21] F. Rutz, P. Kleinow, R. Aidam, W. Bronner, L. Stolch, et al., Proc. SPIE 9974, 99740G (2016).
[22] F. Rutz, R. Aidam, A. Bächle, H. Heußen, W. Bronner, et al., Proc. SPIE 10795, 1079503 (2018).
[23] S. Pellegrini, R. Warburton, L. Tan, J. Ng, A. Krysa, et al., IEEE J. Quant. Electron. 42, 397 (2006).
[24] F. Zappa, A. Tosi and S. Cova, Proc. SPIE 6583, 65830E (2007).
[25] F. Rutz, P. Kleinow, R. Aidam, H. Heussen, W. Bronner, et al., Proc. SPIE 9481, 948107 (2015).